# Two-Dimensional Rotational-Echo Double Resonance of $Val_1$-[1-$^{13}$C]$Gly_2$-[$^{15}$N]$Ala_3$-Gramicidin A in Multilamellar Dimyristoylphosphatidylcholine Dispersions†

Andrew W. Hing* and Jacob Schaefer

*Department of Chemistry, Washington University, St. Louis, Missouri 63130*

*Received October 9, 1992; Revised Manuscript Received April 21, 1993*

ABSTRACT: The dipolar coupling between the $Gly_2$ $^{13}$C-1 carbon and $Ala_3$ $^{15}$N-amide nitrogen was used to investigate the conformation and dynamics of the $Gly_2$-$Ala_3$ $^{13}$C-$^{15}$N peptide bond in $Val_1$-[1-$^{13}$C]$Gly_2$-[$^{15}$N]$Ala_3$-gramicidin A incorporated into multilamellar dispersions of dimyristoylphosphatidylcholine. Measurement of the $^{13}$C–$^{15}$N dipolar coupling constant $D$ of the labeled gramicidin in a powder and the effective dipolar coupling constant $D_e$ in a multilamellar dispersion was accomplished by two-dimensional rotational-echo double-resonance (2D REDOR) NMR, a magic-angle spinning experiment designed to measure weak dipolar coupling constants. The magnitudes of $D$ and $D_e$ were measured by the mirror-symmetric form of 2D REDOR, and the signs of $D$ and $D_e$ were determined relative to the sign of the isotropic indirect spin–spin coupling constant $J$ by the mirror-asymmetric form of 2D REDOR. From knowledge of the magnitudes of $D$ and $D_e$, four possible values were calculated for the angle between the $Gly_2$-$Ala_3$ $^{13}$C–$^{15}$N peptide bond and the gramicidin helical axis. Additional knowledge of the signs of $D$ and $D_e$ permitted the set of possible values for the peptide bond angle to be reduced to a single angle and its supplement (64°, 116°). This information about the $Gly_2$-$Ala_3$ $^{13}$C–$^{15}$N peptide bond angle eliminates the double-stranded, helical dimers and the left-handed, single-stranded, $\beta^{6.3}$ helical dimer but supports the right-handed, single-stranded, $\beta^{6.3}$ helical dimer as the structural model for gramicidin in multilamellar dispersions.

$Val_1$-gramicidin A is a linear pentadecapeptide that has the following primary structure (Sarges & Witkop, 1965):

HCO-L-$Val_1$-$Gly_2$-L-$Ala_3$-D-$Leu_4$-L-$Ala_5$-D-$Val_6$-L-$Val_7$-D-$Val_8$-L-$Trp_9$-D-$Leu_{10}$-L-$Trp_{11}$-D-$Leu_{12}$-L-$Trp_{13}$-D-$Leu_{14}$-L-$Trp_{15}$-$NHCH_2CH_2OH$

Because gramicidin forms ion channels in model membranes (Hladky & Haydon, 1970, 1972), gramicidin has been studied as a potential model of ion channels in cell membranes. However, an understanding of how gramicidin conducts ions requires knowledge of the three-dimensional structure of gramicidin in membranes. Consequently, many techniques have been used to obtain structural information about gramicidin in a lipid environment. Some of the most informative techniques have been provided by the field of solid-state NMR.[1]

In solid-state NMR studies of gramicidin in oriented bilayers, nuclear spin interactions that have been examined include the $^{13}$C chemical shift anisotropy (Cornell et al., 1988; Smith et. al., 1989), the $^{13}$C–$^{13}$C dipolar interaction (Cornell et al., 1988), the $^{15}$N chemical shift anisotropy (Nicholson et al., 1987; Fields et al., 1988; Nicholson & Cross, 1989), the $^{15}$N–$^{1}$H dipolar interaction (LoGrasso et al., 1989), the $^{15}$N–$^{13}$C dipolar interaction (Teng et al., 1991), and the $^{2}$H quadrupolar interaction (Hing et al., 1990a,b). The results of these studies provide strong evidence that gramicidin forms a single-stranded, $\beta^{6.3}$ helical dimer (Urry, 1971; Urry et al., 1971; Arseniev et al., 1986; Venkatachalam & Urry, 1983) in oriented bilayers and that the helices are right-handed (Nicholson & Cross, 1989).

Fewer solid-state NMR experiments have been performed on gramicidin in multilamellar dispersions. In these systems, the isotropic distribution of molecular orientations generates so-called powder pattern spectra. Powder patterns representing motionally averaged nuclear spin interactions yield information about bond angles relative to the helical axis when fast axial rotation and coincidence of the motional and helical axes are assumed. Measurements of gramicidin based on the $^{13}$C or $^{15}$N chemical shift interaction (Smith & Cornell, 1986; Killian et al., 1988; Nicholson et al., 1991), however, require independent knowledge of the orientation of the principal axis system of the chemical shift tensor relative to the molecular frame. Furthermore, when the static shift tensor is axially asymmetric, two unknown parameters must be evaluated even though measurement of a motionally averaged, chemical shift powder pattern yields only a single piece of information (Seelig, 1978). In this case, such a measurement can only indicate that the actual bond angle lies within a certain angular range.

More definitive determinations of gramicidin bond angles in multilamellar dispersions are provided by measurements based on the $^{2}$H quadrupolar interaction (Datema et al., 1986; Prosser et al., 1991). Bond angle determinations are more definitive in this case because the unique axis of the principal axis system of the electric field gradient (EFG) tensor is generally the same as the bond vector connected to the $^{2}$H atom and because the EFG tensor is effectively axially symmetric thereby requiring that only a single unknown parameter be evaluated from a single measurement (Seelig, 1977). Measurements of powder patterns representing mo-

† This work was supported by NSF Grant DIR-8720089. A.W.H. gratefully acknowledges support from the Monsanto Co.

* To whom correspondence should be addressed.

[1] Abbreviations: NMR, nuclear magnetic resonance; 2D REDOR, two-dimensional rotational-echo double resonance; CP, cross polarization; MAS, magic-angle spinning; CPMAS, cross-polarization magic-angle spinning; $T_r$, rotor period; DMPC, dimyristoylphosphatidylcholine; HPLC, high-performance liquid chromatography; TLC, thin-layer chromatography; TMS, tetramethylsilane.

0006-2960/93/0432-7593$04.00/0 

tionally averaged quadrupolar splittings arising from exchange-labeled gramicidin molecules indicate that N–$^2$H bonds form angles of 16°, 25°, and 35° or 90° relative to the motional axis (Datema et al., 1986). Similar measurements performed on selectively deuterated gramicidin molecules indicate that $C_\alpha$–$^2$H bond angles relative to the motional axis do not deviate by more than 5° from the values predicted by a best-fit model of a $\beta^{6.3}$ helical dimer (Prosser et al., 1991). These results provide strong evidence that gramicidin forms a single-stranded, $\beta^{6.3}$ helical dimer in multilamellar dispersions. Furthermore, Prosser et al. have used the average of the ratio of the quadrupolar splittings of the L residues to those of the D residues to argue that the $\beta^{6.3}$ helices are right-handed.

In this paper, a recently developed solid-state NMR technique is used to investigate further the structure of gramicidin in multilamellar dispersions. Specifically, the mirror-symmetric and mirror-asymmetric versions of the two-dimensional rotational-echo double-resonance (2D REDOR) experiment (Gullion et al., 1988; Gullion & Schaefer, 1989) are used to measure the $^{13}$C–$^{15}$N dipolar coupling constant of a directly bonded pair of isotopically enriched nuclei in gramicidin incorporated into multilamellar dispersions. These 2D REDOR experiments are magic-angle spinning (MAS) experiments that are designed to measure weak heteronuclear dipolar coupling constants quantitatively. The use of the dipolar interaction to study structure and dynamics has the advantage that conclusions about the dipolar tensor can be related directly to the molecular frame. These comparisons are possible because the unique axis of the dipolar tensor and the internuclear axis coincide. Furthermore, because the dipolar tensor is exactly axially symmetric, measurement of the dipolar coupling constant allows specific values instead of angular ranges to be derived for the actual bond angle.

The $^{13}$C–$^{15}$N bond of gramicidin studied in this paper is the $^{13}$C–$^{15}$N peptide linkage between the $Gly_2$ residue and the $Ala_3$ residue in isotopically enriched $Val_1$-gramicidin A. Gramicidin A molecules containing isotopically enriched $Gly_2$ $^{13}$C-1 carbon atoms and $Ala_3$ $^{15}$N-amide nitrogen atoms were incorporated into multilamellar dispersions composed of DMPC and studied at a temperature above the phase transition temperature of the lipid. Under these conditions, the $Gly_2$-$Ala_3$ $^{13}$C–$^{15}$N peptide bond undergoes motional averaging that reduces the effective strength of the $^{13}$C–$^{15}$N dipolar interaction. Mirror-symmetric 2D REDOR experiments measure the magnitude of this effective $^{13}$C–$^{15}$N dipolar coupling constant in a multilamellar dispersion and the magnitude of the $^{13}$C–$^{15}$N dipolar coupling constant in a powder to yield a set of two angles and their respective supplements as possibilities for the actual angle between the $^{13}$C–$^{15}$N bond and the helical axis. Furthermore, mirror-asymmetric 2D REDOR experiments described in this paper demonstrate how the sign of the effective $^{13}$C–$^{15}$N dipolar coupling constant in a multilamellar dispersion and the sign of the $^{13}$C–$^{15}$N dipolar coupling constant in a powder can be determined relative to the sign of the isotropic indirect spin–spin coupling constant. This yields information about the relative sign of these dipolar coupling constants and permits the set of possible bond angles to be reduced to a single angle and its supplement. The resulting information about the conformation of the $Gly_2$-$Ala_3$ $^{13}$C–$^{15}$N peptide bond allows conclusions to be reached about the structure of gramicidin in multilamellar dispersions.

## EXPERIMENTAL PROCEDURES

*Peptide Synthesis.* Isotopic enrichment of the nuclei involved in the $^{13}$C–$^{15}$N peptide linkage between the $Gly_2$ residue and the $Ala_3$ residue in $Val_1$-gramicidin A was achieved by replacing $Gly_2$ with [1-$^{13}$C]$Gly_2$ and by replacing $Ala_3$ with [$^{15}$N]$Ala_3$. The procedure used to incorporate [1-$^{13}$C]-glycine (99 atom % $^{13}$C, MSD Isotopes) and [$^{15}$N]alanine (99 atom % $^{15}$N, MSD Isotopes) into gramicidin A and the procedure used to purify the crude peptide have been described previously (Hing et al., 1990a). The synthesis of pure $Val_1$-[1-$^{13}$C]$Gly_2$-[$^{15}$N]$Ala_3$-gramicidin A was verified by HPLC, TLC, $^{13}$C NMR, mass spectrometry, and amino acid analysis performed in the same fashion as described before (Hing et al., 1990a,b).

*Sample Preparation.* The procedure for incorporating $Val_1$-[1-$^{13}$C]$Gly_2$-[$^{15}$N]$Ala_3$-gramicidin A into multilamellar dispersions composed of DMPC followed that described for incorporating gramicidin A into oriented DMPC bilayers up to the point of hydration (Hing et al., 1990a). At this point, after the 10:1 molar ratio lipid/peptide deposits had been dried under vacuum for 2 days, the lipid/peptide deposits were placed into sample containers designed to permit liquids to be spun inside a MAS rotor. An excess of distilled, deionized water was then added to each sample container to produce a molar ratio of water to DMPC in the 80:1 to 110:1 range. The samples were then repeatedly subjected to a cycle consisting of vortexing, freezing, and thawing. Finally, the samples were heated at 43 °C for at least 4 days.

### *NMR*

*NMR Console and Probe.* Observation of $^{13}$C nuclei was performed with a home-built spectrometer that is capable of producing radio frequency pulses at three different frequencies with the field strength of the pulses regulated from scan to scan. The NMR probe used to observe the $^{13}$C signals was a triply-tuned, transmission line probe built by R. A. McKay (U.S. Patent 4,446,431). The probe allows high-power radio frequency pulses to be applied at 200 ($^1$H), 50 ($^{13}$C), and 20 MHz ($^{15}$N). The probe also allows samples to be spun at the magic-angle at speeds up to 4 kHz. Observation of $^{31}$P nuclei was performed with a similar, four-channel instrument that allows signals at 81 MHz ($^{31}$P) to be observed.

Temperature control was achieved by regulating the temperature of the air that drives the journal bearings. For samples in powder form, data were acquired at room temperature. For multilamellar dispersions, data were acquired at a temperature well above the phase transition temperature of approximately 28 °C (Chapman et al., 1974, 1977; Nicholson et al., 1987).

*$^{31}$P NMR.* Phosphorus NMR data of a nonspinning sample of multilamellar dispersions were obtained with a phase-cycled Hahn-echo experiment (Rance & Byrd, 1983). The $^{31}$P 90° pulse width was 6.6 μs, the interpulse delay was 24 μs, the recycle delay was 1 s, and the strength of the $^1$H decoupling field was 60 kHz. Spectra were acquired with a spectral width of 10 000 Hz and a spectral size of 2048 complex points and were plotted with a line broadening of 80 Hz. The 0 ppm reference point of the spectra was set equal to the isotropic resonance frequency, as determined by room temperature $^{31}$P CPMAS experiments, of external DMPC in powder form.

*$^{13}$C CPMAS.* Carbon-13 CPMAS spectra were acquired at a MAS speed of $1/T_r$ = 1000 Hz with quadrature phase cycling and spin temperature alternation. Spectra were referenced to an external TMS standard and were acquired with a spectral width of 20 000 Hz and a recycle delay of 1 s. For samples in powder form, cross polarization from $^1$H to $^{13}$C was performed at a field strength of 35 kHz with a contact time of 2 ms; the strength of the $^1$H decoupling field

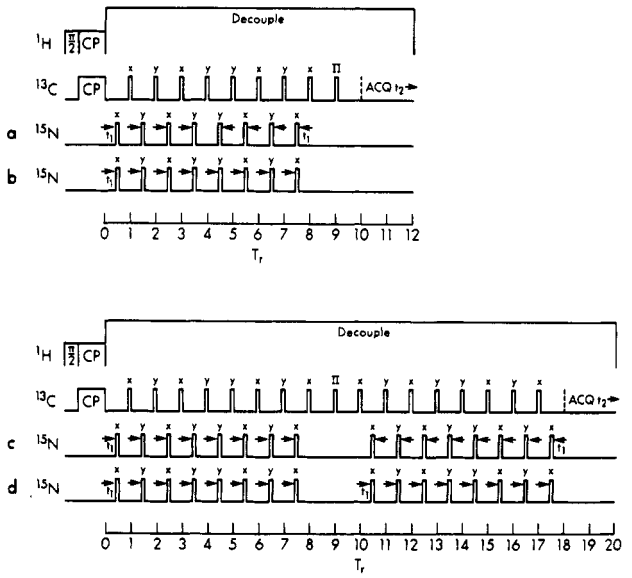


FIGURE 1: 2D REDOR pulse sequences. The mirror-symmetric experiment with (a) 8 and (c) 16 rotor periods of effective dephasing and the mirror-asymmetric experiment with (b) 8 and (d) 16 rotor periods of effective dephasing are diagrammed.

was 100 kHz; the spectral size was 1024 complex points; and line broadening of 40 Hz was used to process spectra. For samples of multilamellar dispersions, cross polarization from $^1$H to $^{13}$C was performed at a field strength of 38 kHz with a contact time of 2 ms; the strength of the $^1$H decoupling field was 60 kHz; the spectral size was 2048 complex points; and line broadening of 20 Hz was used to process spectra.

*$^{13}$C-Observed, $^{15}$N-Dephased 2D REDOR.* The mirror-symmetric and mirror-asymmetric 2D REDOR pulse sequences used in this paper are diagrammed in Figure 1. The initial cross polarization from protons to carbons is followed by a train of $^{13}$C $\pi$ pulses each of which is applied at the end of a rotor period, a train of $^{15}$N $\pi$ pulses each of which is applied at a time $t_1$ from the start or end of a rotor period, and high-power proton decoupling. In the mirror-symmetric sequences (Figure 1a,c), the second set of $^{15}$N $\pi$ pulses is incremented in a direction opposite to that of the first set. In the mirror-asymmetric sequences (Figure 1b,d), all the $^{15}$N $\pi$ pulses are incremented in the same direction. The application of a train of $\pi$ pulses to both $^{13}$C and $^{15}$N nuclei and phase alternation of each $\pi$ pulse train according to an XY-8, compensated Carr–Purcell scheme (Gullion et al., 1990) are modifications of the original 2D REDOR sequence (Gullion et al., 1988; Gullion & Schaefer, 1989) that have been described before (Gullion et al., 1990). The addition of a $^{13}$C $\pi$ pulse (denoted by $\Pi$ in the sequences of Figure 1) to the XY-8 train of $^{13}$C $\pi$ pulses is required for full implementation of the XY-8 phase alternation scheme. Over the time period beginning one rotor period before the $\Pi$ pulse and ending one rotor period after the $\Pi$ pulse, the net phase accumulated due to isotropic and anisotropic chemical shift interactions and heteronuclear dipolar and indirect spin–spin interactions is zero. Therefore, the total number of rotor periods of dephasing is two less than the total number of rotor periods between the $^{13}$C CP pulse and data acquisition. Acquisition of the $^{13}$C free induction decay occurs during the second time dimension $t_2$.

Two-dimensional REDOR spectra were acquired at a MAS speed of $1/T_r$ = 1000 Hz with the $^{13}$C and $^{15}$N carrier frequencies placed on resonance for the nuclei of interest. The phases of the XY-8 $\pi$ pulses were left unchanged while phase cycling of the $^{13}$C CP pulse, the $\Pi$ pulse, and the receiver followed the scheme of Rance & Byrd, 1983. The spin temperature was alternated between consecutive executions of this phase-cycling scheme. Cross polarization from $^1$H to $^{13}$C was performed at a field strength of 38 kHz with a contact time of 2 ms. The 90° pulse width was 6.6 $\mu$s for $^1$H, $^{13}$C, and $^{15}$N. The $^{13}$C spectra were referenced to an external TMS standard and were acquired with a spectral width of 20 000 Hz, a spectral size of 2048 complex points, and a recycle delay of 1 s. For samples in powder form, 2D REDOR spectra were acquired with $N_c$ = 8 rotor periods of effective dephasing (Figure 1a,b); $^{15}$N $\pi$ pulse placement as measured by $t_1$ was incremented in steps of $T_r/50$; the strength of the $^1$H decoupling field was 100 kHz; and line broadening of 40 Hz was used to process spectra. For samples of multilamellar dispersions, 2D REDOR spectra were acquired with $N_c$ = 16 rotor periods of effective dephasing (Figure 1c,d); $^{15}$N $\pi$ pulse placement was incremented in steps of $T_r/32$; the strength of the $^1$H decoupling field was 60 kHz; and line broadening of 20 Hz was used to process spectra. For powder samples and multilamellar dispersions, a greater number of scans was used to acquire 2D REDOR spectra when magnetization was observed to change rapidly as a function of $t_1$ because magnetization behavior in this $t_1$ time-domain region contains most of the information about the value of the dipolar coupling constant.

## THEORY

*Basic Principles.* The 2D REDOR experiment is based upon the creation of an average dipolar interaction and an average indirect spin–spin interaction between two heteronuclear spins, I and S, under conditions of MAS (Gullion & Schaefer, 1989). These average interactions are created by the appropriate application of $\pi$ pulses. The spin system then evolves under the influence of the average dipolar and indirect spin–spin interactions at an average angular frequency that is determined by the placement of the $\pi$ pulses. This average angular frequency of evolution ultimately determines the amount of magnetization that is observed.

*Powder Samples.* In the relatively immobile environment of a powder, the observable magnetization $M_S$ for an isotropic distribution of I–S internuclear vector orientations is obtained by summation of the magnetization components for a single orientation and is given by

$$M_S = (1/4\pi)\int_{\alpha=0}^{2\pi}\int_{\beta=0}^{\pi}\cos(\bar{\omega}(\alpha,\beta)N_cT_r)\sin\beta\,d\beta\,d\alpha \quad (1)$$

where $\bar{\omega}(\alpha,\beta)$ is the average angular frequency of evolution for the $\alpha$, $\beta$ orientation in rad/s, $N_c$ is the total number of rotor periods of dephasing, and $T_r$ is the rotor period in seconds. The symbols $\alpha$ and $\beta$ are the azimuthal and polar angles, respectively, of the I–S internuclear vector's initial orientation relative to the rotor axis.

Since $\bar{\omega}(\alpha,\beta)$ is determined by the placement of the $\pi$ pulses, the average angular frequency created by the mirror-symmetric 2D REDOR sequence (Gullion et al., 1988; Gullion & Schaefer, 1989)

$$\bar{\omega}(\alpha,\beta) = \pm\{(D/2)[2\sqrt{2}\sin 2\beta\sin\alpha\,[\cos\omega_r t_1 - 1] - \sin^2\beta\sin 2\alpha\,[\cos 2\omega_r t_1 - 1]]\} \quad (2)$$

is different from the average angular frequency created by the mirror-asymmetric sequence (original equation given by Gullion & Schaefer, 1989; presented here in corrected form)

$$\bar{\omega}(\alpha,\beta) = \pm\{(D/2)[2\sqrt{2}\sin 2\beta\,[\sin(\alpha+\omega_r t_1)-\sin\alpha]-\sin^2\beta\,[\sin(2\alpha+2\omega_r t_1)-\sin 2\alpha]]+J(\omega_r t_1-\pi)\} \quad (3)$$

where $D$ is the coupling constant that characterizes the dipolar interaction between the I spin and S spin in the powder (in hertz), and $J$ is the coupling constant that characterizes the isotropic indirect spin–spin interaction between those same two spins (in hertz). The symbol $\omega_r = 2\pi/T_r$ is the MAS speed in rad/s, and $t_1$ measures the position of the $^{15}N$ $\pi$ pulses in seconds. Examination of eqs 1–3 shows that the average angular frequency's magnitude $|\bar{\omega}(\alpha,\beta)|$ and therefore the observable magnetization $M_S$ reflect only the magnitude of $D$ when the mirror-symmetric sequence is applied to a powder sample but reflect both the magnitudes of $D$ and $J$ and their relative sign when the mirror-asymmetric sequence is applied.

In principle, the pure dipolar coupling constant for absolutely motionless molecules can be calculated from the following equation:

$$D = \gamma_I\gamma_S h/4\pi^2 r^3 \quad (4)$$

where $D$ is in hertz, $\gamma_I$ is the gyromagnetic ratio of the I spin, $\gamma_S$ is the gyromagnetic ratio of the S spin, $h$ is Planck's constant, and $r$ is the internuclear distance. However, measured values of $D$ often differ from theoretical values because of the presence of motion or other factors.

*Multilamellar Dispersions.* In the liquid-crystalline phase of multilamellar dispersions, the I–S internuclear vector rotates rapidly about a motional axis. The observable magnetization for such a system can be calculated by unitary transformation of the dipolar tensor from its principal axis system to the motional axis frame, transformation from the motional axis frame to the rotor frame, and then transformation from the rotor frame to the laboratory frame. The resulting equations can be simplified because the I–S internuclear vector rotates about the motional axis at a rate ($\gg 10^5$ Hz) much greater than typical MAS speeds ($\sim 10^3$ Hz) and much greater than typical values of weak dipolar coupling constants ($\lesssim 10^3$ Hz). In this case, the observable magnetization $M_S$ for an isotropic distribution of motional axis orientations is given by

$$M_S = (1/4\pi)\int_{\alpha'=0}^{2\pi}\int_{\beta'=0}^{\pi}\cos(\bar{\omega}(\theta,\alpha',\beta')N_c T_r)\sin\beta'\,d\beta'\,d\alpha' \quad (5)$$

where $\bar{\omega}(\theta,\alpha',\beta')$ is the average angular frequency of evolution for the $\theta,\alpha',\beta'$ orientation in rad/s. The symbol $\theta$ is the polar angle between the I–S internuclear vector and the motional axis, and the symbols $\alpha'$ and $\beta'$ are the azimuthal and polar angles, respectively, of the initial orientation of the motional axis relative to the rotor axis.

The average angular frequency $\bar{\omega}(\theta,\alpha',\beta')$ created by the mirror-symmetric 2D REDOR sequence in a system undergoing fast rotation about a motional axis is given by

$$\bar{\omega}(\theta,\alpha',\beta') = \pm\{(D_e/2)[2\sqrt{2}\sin 2\beta'\sin\alpha'\,[\cos\omega_r t_1-1]-\sin^2\beta'\sin 2\alpha'\,[\cos 2\omega_r t_1-1]]\} \quad (6)$$

while the average angular frequency $\bar{\omega}(\theta,\alpha',\beta')$ created by the mirror-asymmetric sequence is given by

$$\bar{\omega}(\theta,\alpha,'\beta') = \pm\{(D_e/2)[2\sqrt{2}\sin 2\beta'\,[\sin(\alpha'+\omega_r t_1)-\sin\alpha']-\sin^2\beta'\,[\sin(2\alpha'+2\omega_r t_1)-\sin 2\alpha']]+J(\omega_r t_1-\pi)\} \quad (7)$$

The effective coupling constant $D_e$ (in hertz) depends on $\theta$ and characterizes the effective strength of the dipolar interaction between the I spin and S spin in systems undergoing fast rotation about a motional axis. As before, the coupling constant $J$ characterizes the isotropic indirect spin–spin interaction between those same two spins. Examination of eqs 5–7 shows that the average angular frequency's magnitude $|\bar{\omega}(\theta,\alpha',\beta')|$ and therefore the observable magnetization $M_S$ are determined by the magnitude of $D_e$ when the mirror-symmetric sequence is applied and are determined by the magnitudes of $D_e$ and $J$ and their relative sign when the mirror-asymmetric sequence is applied.

The equation for $D_e$ in terms of $\theta$ is given by

$$D_e = D(3\cos^2\theta - 1)/2 \quad (8)$$

which permits the effective dipolar coupling constant in the membrane, $D_e$, to be related directly to the dipolar coupling constant in the powder, $D$. Clearly, $D_e$ and $D$ can possess identical or opposite signs depending on the value of $\theta$. The use of the powder dipolar coupling constant $D$ in eq 8 as the reference for calculating $D_e$ is predicated on two assumptions. The first assumption is that the I–S internuclear distance is the same in the liquid-crystalline phase and the powder. This assumption is certainly true for a one-bond I–S spin pair. The second assumption is that small-amplitude, high-frequency motions in the liquid-crystalline phase do not differ significantly from those in the powder and therefore do not cause the reference dipolar coupling constant to differ significantly from $D$. This is certainly a valid premise if eq 8 is used to calculate values for the angle $\theta$ when $D_e \ll D$ because potential deviations of the reference dipolar coupling constant from $D$ do not essentially affect $\theta$ values calculated from eq 8 when $D_e \ll D$.

The use of the same isotropic indirect spin–spin coupling constant, $J$, in the mirror-asymmetric, average angular frequency equation for a powder sample (eq 3) and in the analogous equation for a multilamellar dispersion (eq 7) is based on the assumption that the isotropic indirect spin–spin interaction is unchanged by incorporation into a liquid-crystalline phase from a powder. This assumption is valid for the isotropic indirect spin–spin interaction between directly amide-bonded $^{13}C$ and $^{15}N$ nuclei because effects of solvent, protonation, conformation, and hydrogen-bond formation are not expected to change the sign of the isotropic indirect spin–spin coupling constant, and are not expected to alter its magnitude by more than $\sim 10\%$, a percentage change that is negligible for the purposes of this paper (Witanowski et al., 1986; Kricheldorf, 1980; Irving & Lapidot, 1976; Walter & Wright, 1979; Kainosho et al., 1987).

Examination of eqs 3 and 7 shows that the isotropic indirect spin–spin coupling constant, unlike the dipolar coupling constant, is not effectively scaled by the rapid axial rotation found in the liquid-crystalline phase. Frequencies generated by the isotropic indirect spin–spin interaction, unlike those generated by the dipolar interaction, are independent of orientation and are therefore unaffected by rotational motion.

If, in addition to the dipolar and isotropic indirect spin–spin couplings, an anisotropic indirect spin–spin coupling exists between directly bonded spins, the argument can be made (Power & Wasylishen, 1991) that the tensor describing the one-bond, anisotropic indirect spin–spin interaction is axially symmetric and is oriented with its unique axis parallel to the unique axis of the one-bond dipolar tensor. In this case, the presence of an anisotropic indirect spin–spin interaction would only affect the values measured for $D_e$ and $D$ and would do so in a way that leaves the value of $D_e/D$ unchanged. Thus, the existence of a one-bond, anisotropic indirect spin–spin

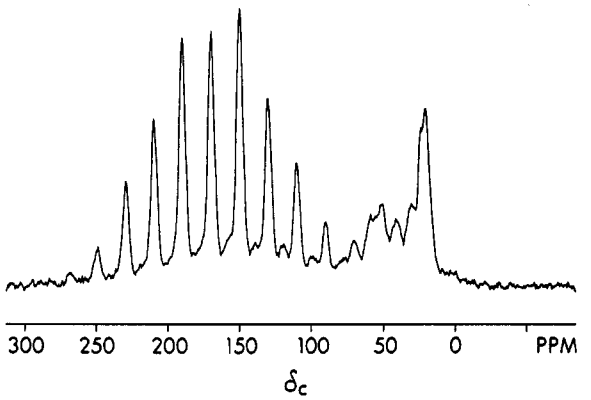


FIGURE 2: $^{13}$C CPMAS spectrum of the powder form of $Val_1$-[1-$^{13}$C]$Gly_2$-[$^{15}$N]$Ala_3$-gramicidin A (69 mg) at room temperature. The spectrum was acquired at $1/T_r$ = 1000 Hz with 20 000 scans.

coupling would not have any practical effect on theory or measured $\theta$ values.

## RESULTS

### *Gramicidin Powder*

*$^{13}$C CPMAS NMR.* The $^{13}$C CPMAS spectrum of the powder form of $Val_1$-[1-$^{13}$C]$Gly_2$-[$^{15}$N]$Ala_3$-gramicidin A is shown in Figure 2. The sideband pattern representing the chemical shift anisotropy of the enriched $^{13}$C-1 carbon atom of $Gly_2$ is centered at the isotropic resonance frequency of 170 ppm and dominates the 60–270 ppm region. Peaks representing natural-abundance $^{13}$C carbonyl and aromatic carbons of the other residues are present at the base of the $Gly_2$ $^{13}$C-1 peaks. Natural-abundance $^{13}$C peaks representing other types of carbon atoms present in the peptide are evident in the 0–60 ppm region.

*Mirror-Symmetric 2D REDOR.* Mirror-symmetric, $^{13}$C-observed, $^{15}$N-dephased 2D REDOR spectra of the powder form of $Val_1$-[1-$^{13}$C]$Gly_2$-[$^{15}$N]$Ala_3$-gramicidin A are shown in Figure 3. As the placement of $^{15}$N $\pi$ pulses is incremented across the rotor cycle, acquired $^{13}$C spectra progress from the spectrum displayed in Figure 3a ultimately to the spectrum displayed in Figure 3j. These spectra show that ten rotor cycles after cross polarization, the $Gly_2$ carbonyl carbons still possess peaks of significant intensity. Furthermore, only the $Gly_2$ carbonyl-carbon sideband pattern is modulated as the placement of the $^{15}$N $\pi$ pulses is changed.

The total magnetization for each $t_1$ point is obtained by integration of the spectral region containing the $Gly_2$ carbonyl-carbon sideband pattern and is plotted in Figure 4a as a solid circle. The real Fourier transform of the experimental data points in Figure 4a is plotted in Figure 4b. The modulation of the observed magnetization in Figure 4a and the pattern of sidebands in Figure 4b arise solely from dipolar modulation of the $Gly_2$ $^{13}$C-1 carbon by the $Ala_3$ $^{15}$N-amide nitrogen. The natural-abundance $^{13}$C carbons of the other residues contribute only a constant component to the data points in Figure 4a and only centerband intensity at zero frequency to the Fourier transform in Figure 4b. More importantly, because magnetization generated by the mirror-symmetric sequence obeys eqs 1 and 2, the data in Figures 4a and 4b are sensitive only to the magnitude of the dipolar coupling constant $|D|$ between the $Gly_2$ $^{13}$C-1 carbon and the $Ala_3$ $^{15}$N-amide nitrogen in this powder sample.

The experimental data in Figure 4 can be analyzed by comparison of the data to theoretical, mirror-symmetric simulations. The simulation of the $t_1$ time domain (Figure 4a, solid line) shows that total magnetization changes most

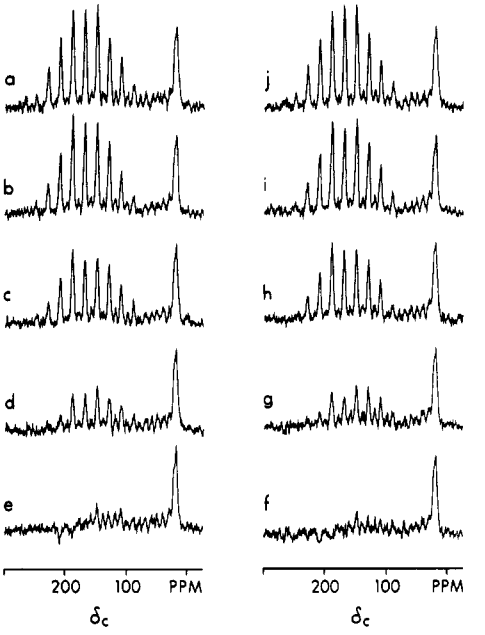


FIGURE 3: Mirror-symmetric 2D REDOR spectra of the powder form of $Val_1$-[1-$^{13}$C]$Gly_2$-[$^{15}$N]$Ala_3$-gramicidin A (69 mg) at room temperature. Mirror-symmetric spectra were acquired according to the pulse sequence diagrammed in Figure 1a at $1/T_r$ = 1000 Hz with $N_c$ = 8 and $t_1/T_r$ incremented from 1/50 to 49/50 in steps of 1/50. All spectra from $t_1/T_r$ = 1/50 to 49/50 were acquired with 9152 scans. Figure 3 displays the spectra corresponding to $t_1/T_r$ = (a) 1/50, (b) 2/50, (c) 3/50, (d) 4/50, (e) 5/50, (f) 45/50, (g) 46/50, (h) 47/50, (i) 48/50, and (j) 49/50.

rapidly as a function of $t_1$ during the decay into increasingly smaller oscillations beginning at $t_1/T_r = 0$ and during the rise from increasingly larger oscillations ending at $t_1/T_r = 1$. The rate at which the magnetization changes as a function of $t_1$ in these regions is reflected in the overall width of the corresponding, simulated Fourier transform (Figure 4c). According to eqs 1 and 2, much of the magnetization behavior in the aforementioned, beginning and end regions of the time-domain plot, in contrast to behavior in the central region of the plot, is attributable to orientations $\alpha$, $\beta$ whose average dipolar frequencies $\bar{\omega}(\alpha,\beta)$ change most rapidly as a function of $t_1$. Furthermore, because average dipolar frequency $\bar{\omega}(\alpha,\beta)$ changes with $t_1$ at a rate that is scaled by the value of $|D|$ (see eq 2), those average dipolar frequencies $\bar{\omega}(\alpha,\beta)$ that change most rapidly as a function of $t_1$ are most affected by changes in the value of $|D|$. Consequently, the decay and growth of total magnetization in the beginning and end regions of the time-domain plot (Figure 4a, solid line) and the width of the Fourier transform (Figure 4c) are more sensitive to the value of $|D|$ than oscillations of magnetization and patterns of sidebands in the central regions of the respective plots. Thus, for an isotropic distribution of orientations characterized by a single value of $|D|$, comparison of mirror-symmetric data to theoretical simulations is most meaningful when attention is focused on the extremes of both the time domain and its Fourier transform.

For the mirror-symmetric experimental data shown in Figures 4a (solid circles) and 4b, simulations indicate that the magnetization observed as a function of $t_1$ and its Fourier transform can be characterized by a single value for the magnitude of the dipolar coupling constant. The inset in Figure 4a shows an expanded view of the regions of the $t_1$ time-domain plot considered most relevant for obtaining information about the value of $|D|$. The total error that is plotted for each data point in the inset is obtained by first considering individual sources of error. Uncertainty associated with integration of

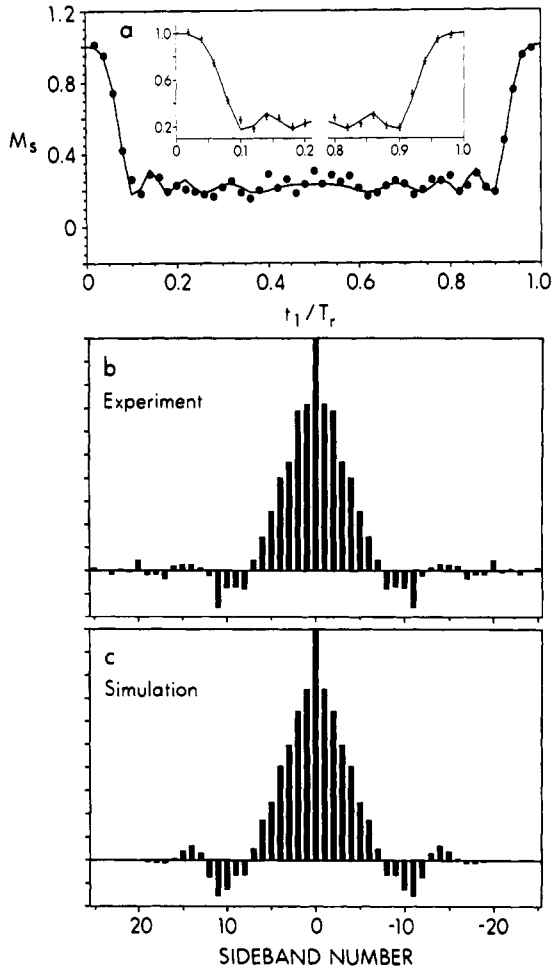


FIGURE 4: Results of the mirror-symmetric experiment performed on the powder form of $Val_1$-[1-$^{13}$C]$Gly_2$-[$^{15}$N]$Ala_3$-gramicidin A (Figure 3). Plotted are the experimentally observed magnetization (a, · · ·) and the simulated magnetization (a, —). Fourier transforms of (a, · · ·) and (a, —) are shown in (b) and (c), respectively. The inset in (a) displays an expanded view of the regions corresponding to $t_1/T_r \leq 0.21$ and $t_1/T_r \geq 0.79$. The total error that is plotted for each data point in the inset is estimated according to the procedure described in the text. The simulations assume that $|D| = 1190$ Hz and that uncoupled $^{13}$C nuclei comprise 19% of the carbons generating signal in the integrated spectral region from 66 to 274 ppm.

noisy spectra is assigned error limits of ~±2 standard deviations based on the standard deviation of the noise from representative portions of the spectral baseline. Uncertainty associated with potential sources of random and systematic errors (such as instrumental instabilities, machine drift, etc.) is judged not to be larger than the uncertainty associated with spectral integration and is therefore assigned approximately the same error limits. The experimental error bars accompanying each data point represent the sum of these contributions. Given these error bars, the experimental data are best matched to a simulation of observed magnetization (Figure 4a, solid line) and a simulated sideband pattern (Figure 4c) that correspond to a dipolar coupling constant of magnitude $|D| = 1190$ Hz, with a maximum uncertainty of ~±2–3% in the measured value of $|D|$. A previous investigation of this sample's dipolar coupling constant measured the same value for $|D|$ (Bork et al., 1990).

Based on eq 4, the magnitude of the pure dipolar coupling constant of a $^{13}$C–$^{15}$N pair separated by a peptide-bond length of $r = 1.33$ Å (Momany et al., 1975) is calculated to be $|D| = 1300$ Hz. The fact that the measured value of the dipolar coupling constant is smaller in magnitude than the theoretical value has been observed before for a $^{13}$C–$^{15}$N pair in a similar

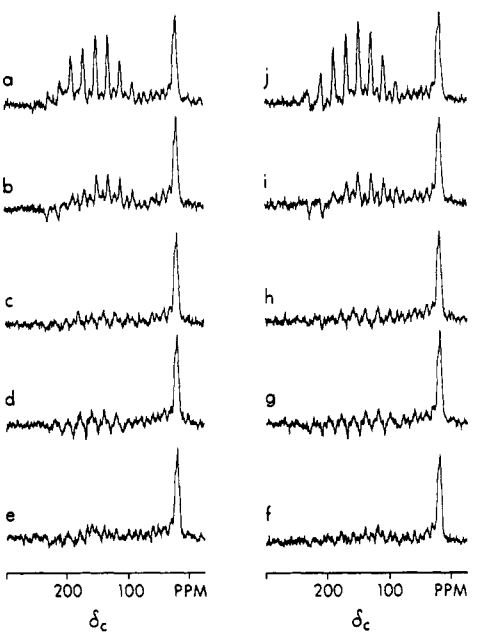


FIGURE 5: Mirror-asymmetric 2D REDOR spectra of the powder form of $Val_1$-[1-$^{13}$C]$Gly_2$-[$^{15}$N]$Ala_3$-gramicidin A (69 mg) at room temperature. Mirror-asymmetric spectra were acquired according to the pulse sequence diagrammed in Figure 1b at $1/T_r = 1000$ Hz with $N_c = 8$ and $t_1/T_r$ incremented from 1/50 to 49/50 in steps of 1/50. Spectra from $t_1/T_r = 1/50$ to 10/50 and 40/50 to 49/50 were acquired with 13,088 scans while spectra from $t_1/T_r = 11/50$ to 39/50 were acquired with 4992 scans. Figure 5 displays the spectra corresponding to $t_1/T_r$ = (a) 1/50, (b) 2/50, (c) 3/50, (d) 4/50, (e) 5/50, (f) 45/50, (g) 46/50, (h) 47/50, (i) 48/50, and (j) 49/50.

amide bond (Hing et al., 1993) and can be explained by the presence of small-amplitude, high-frequency motions.

*Mirror-Asymmetric 2D REDOR.* Mirror-asymmetric 2D REDOR spectra of the powder form of $Val_1$-[1-$^{13}$C]$Gly_2$-[$^{15}$N]$Ala_3$-gramicidin A are shown in Figure 5. As the placement of $^{15}$N $\pi$ pulses is incremented across the rotor cycle, acquired $^{13}$C spectra progress from the spectrum displayed in Figure 5a ultimately to the spectrum displayed in Figure 5j. The mirror-asymmetric sequence, like the mirror-symmetric sequence, results in modulation of only the $Gly_2$ carbonyl-carbon sideband pattern. However, the mirror-asymmetric sequence causes the sideband pattern of the $Gly_2$ carbonyl carbon to change more rapidly as a function of $t_1$.

The magnetization obtained by integration of the spectral region containing the $Gly_2$ carbonyl-carbon sideband pattern is plotted as a function of $t_1$ in Figure 6a as solid circles while the real Fourier transform of these data points is plotted in Figure 6b. Because magnetization generated by the mirror-asymmetric sequence obeys eqs 1 and 3, the data in Figures 6a and 6b are sensitive to the magnitudes and relative sign of the dipolar and isotropic indirect spin–spin coupling constants between the $Gly_2$ $^{13}$C-1 carbon and the $Ala_3$ $^{15}$N-amide nitrogen. Since an indication of the magnitude of the dipolar coupling constant in the powder is provided by the mirror-symmetric experiment, and since, for reasons stated previously, the magnitude of the isotropic indirect spin–spin coupling constant in the powder can be assumed to be equal to the value $|J| = 14.5$ Hz measured from solution-state $^{13}$C NMR spectra acquired to verify the peptide synthesis, the only unknown determinant of the observable magnetization is the relative sign of the dipolar and isotropic indirect spin–spin coupling constants.

Determination of the relative sign of the dipolar and isotropic indirect spin–spin coupling constants can be accomplished by comparison of the experimental data to theoretical, mirror-

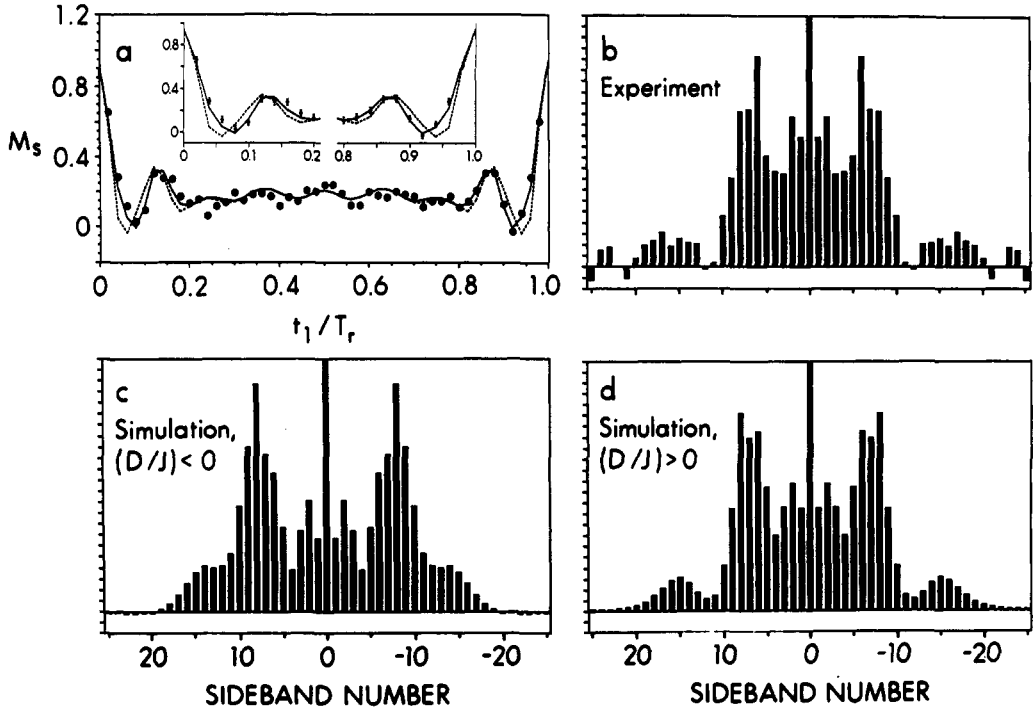


FIGURE 6: Results of the mirror-asymmetric experiment performed on the powder form of Val$_1$-[1-$^{13}$C]Gly$_2$-[$^{15}$N]Ala$_3$-gramicidin A (Figure 5). Plotted are the experimentally observed magnetization (a, • • •), the simulated magnetization for D and J with identical signs (a, —), and the simulated magnetization for D and J with opposite signs (a, - - -). Fourier transforms of (a, • • •), (a, —), and (a, - - -) are shown in (b), (d), and (c), respectively. The inset in (a) displays an expanded view of the regions corresponding to $t_1/T_r \leq 0.21$ and $t_1/T_r \geq 0.79$. The experimental error bars accompanying each data point plotted in the inset are estimated according to the same procedure used to estimate the error bars of Figure 4a. The simulations assume that $|D| = 1150$ Hz and $|J| = 14.5$ Hz and that uncoupled $^{13}$C nuclei comprise 18% of the carbons generating signal in the integrated spectral region from 66 to 274 ppm.

asymmetric simulations. Simulations of the $t_1$ time domain for $D$ and $J$ with identical signs (Figure 6a, solid line) and with opposite signs (Figure 6a, dashed line) show that significant differences exist between the opposite-sign and identical-sign simulations and that such differences occur in the beginning and end regions where the magnetization is changing most rapidly. An expanded view of these regions shows these differences more clearly (Figure 6a, inset). Simulations of the Fourier transform of the $t_1$ time domain for $D$ and $J$ with identical signs (Figure 6d) and with opposite signs (Figure 6c) therefore show that significant differences exist between the two cases in the wings of the Fourier transforms. The fact that the relative sign of $D$ and $J$ significantly affects magnetization behavior even though the magnitude of $J$ is only about one percent of the magnitude of $D$ can be understood in terms of eq 3, the equation for the average angular frequency of the magnetization components comprising the total magnetization. Equation 3 shows that mirror-asymmetric magnetization components do not accumulate phase according to a dipolar frequency characterized by only $D$ and a $J$-coupling frequency characterized by only $J$, but rather accumulate phase according to a $t_1$-dependent average dipolar frequency (eq 3, first expression) and a $t_1$-dependent, average $J$-coupling frequency (eq 3, second expression). Consequently, even if the ratio of $|J|$ to $|D|$ is small, the $t_1$-dependent, average $J$-coupling frequency can be less than, equal to, or greater than the $t_1$-dependent, average dipolar frequency in magnitude and can therefore be a significant factor in determining phase accumulation and magnetization behavior. Furthermore, when the value of $t_1$ causes the average $J$-coupling frequency to be comparable in magnitude to the average dipolar frequency for a given magnetization component, the behavior of that component is then greatly affected by the relative sign of $D$ and $J$. As a result, the total magnetization can be significantly affected by the relative sign of $D$ and $J$ for $t_1$ values in a certain range, and the limits of this range are determined by the relative magnitudes of $D$, $J$, and $N_cT_r$ in eqs 1 and 3. Thus, this $t_1$ value range (for Figure 6a, when $t_1/T_r \lesssim 0.2$ or $\gtrsim 0.8$) and the corresponding region in the Fourier transform (for Figure 6c,d, when sideband number $\gtrsim 8$ or $\lesssim -8$) deserve the most attention when comparisons of mirror-asymmetric data to simulations are performed to determine the relative sign of $D$ and $J$.

Comparison of the mirror-asymmetric experimental data in Figure 6a,b to the simulations in Figure 6a,c,d shows that $D$ and $J$ possess identical signs. This is graphically demonstrated by the inset in Figure 6a which displays the regions of the $t_1$ time domain most sensitive to the relative sign of $D$ and $J$. Moreover, because each magnetization value plotted in the $t_1$ time domain is derived independently (the magnetization values are not artificially symmetrized about $t_1/T_r = 0.5$), each half of the inset in Figure 6a is essentially an independent determination of the relative sign of $D$ and $J$. The inset shows that the simulation for $D$ and $J$ with identical signs clearly falls within the error bars of the experimental data while the simulation for $D$ and $J$ with opposite signs clearly falls outside of the experimental data's error bars.

Further calculations ultimately show that a slightly better fit to the mirror-asymmetric experimental data is obtained when the simulations assume that $|D|$ equals 1150 Hz rather than the value of 1190 Hz used in the mirror-symmetric simulations. However, these calculations also show that mirror-asymmetric simulations based on $|D| = 1150$ Hz exhibit the same essential behavior as those based on $|D| = 1190$ Hz. Thus, simulations based on either value of $|D|$ lead to the same mirror-asymmetric data analysis and the same relative sign determination of $D$ and $J$.

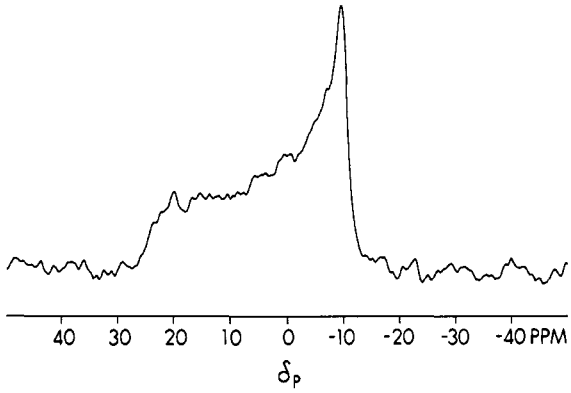


FIGURE 7: $^{31}$P Hahn-echo spectrum of a nonspinning, multilamellar DMPC dispersion containing 1 mg of Val$_1$-[1-$^{13}$C]Gly$_2$-[$^{15}$N]Ala$_3$-gramicidin A at $T$ = 42 °C. The spectrum was acquired with 116 496 scans.

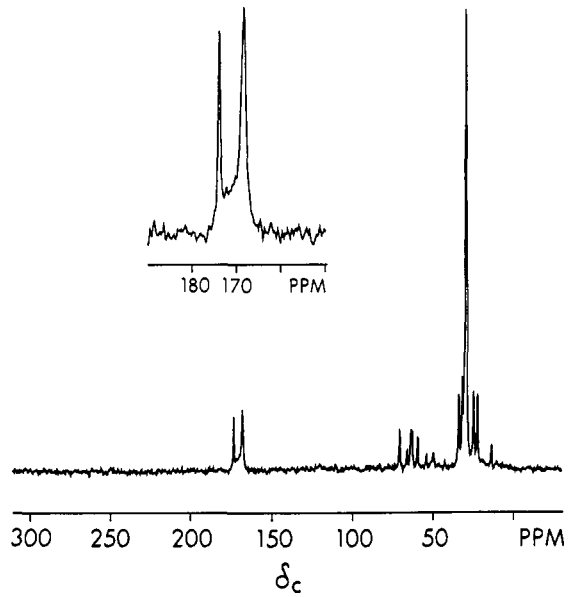


FIGURE 8: $^{13}$C CPMAS spectrum of a multilamellar DMPC dispersion containing 27 mg of Val$_1$-[1-$^{13}$C]Gly$_2$-[$^{15}$N]Ala$_3$-gramicidin A at $T$ = 44 °C. The spectrum was acquired at $1/T_r$ = 1000 Hz with 5000 scans.

### *Gramicidin in Multilamellar DMPC Dispersions*

*$^{31}$P NMR.* The $^{31}$P Hahn-echo spectrum of a liquid-crystalline, multilamellar DMPC dispersion containing Val$_1$-[1-$^{13}$C]Gly$_2$-[$^{15}$N]Ala$_3$-gramicidin A is shown in Figure 7. The characteristic line shape displayed by this spectrum indicates that a single bilayer phase is present above the phase transition temperature (Seelig, 1978).

*$^{13}$C CPMAS NMR.* The $^{13}$C CPMAS spectrum of Val$_1$-[1-$^{13}$C]Gly$_2$-[$^{15}$N]Ala$_3$-gramicidin A in a liquid-crystalline, multilamellar DMPC dispersion is shown in Figure 8. In addition to the peaks representing the carbon atoms of the peptide, peaks representing lipid carbon atoms are also present. In the carbonyl-carbon region of the spectrum, most of the peak centered at the isotropic resonance frequency of 169 ppm represents enriched Gly$_2$ carbonyl carbons while most of the peak found at 174 ppm represents lipid carbonyl carbons. At the base of these two main resonances are peaks representing other $^{13}$C carbonyl carbons at natural abundance. Comparison of the spectrum in Figure 8 with the spectrum in Figure 2 shows that the observed size of the Gly$_2$ carbonyl-carbon chemical shift anisotropy is much smaller for gramicidin incorporated into a multilamellar dispersion than for gramicidin in powder form. This is consistent with previous

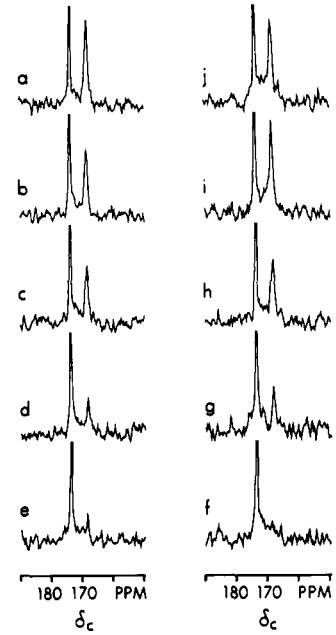


FIGURE 9: Mirror-symmetric 2D REDOR spectra of a multilamellar DMPC dispersion containing 34 mg of Val$_1$-[1-$^{13}$C]Gly$_2$-[$^{15}$N]Ala$_3$-gramicidin A at $T$ = 43 °C. Mirror-symmetric spectra were acquired according to the pulse sequence diagrammed in Figure 1c at $1/T_r$ = 1000 Hz with $N_c$ = 16 and $t_1/T_r$ incremented from 1/32 to 31/32 in steps of 1/32. All spectra from $t_1/T_r$ = 1/32 to 31/32 were acquired with 8000 scans. Figure 9 displays the spectra corresponding to $t_1/T_r$ = (a) 1/32, (b) 2/32, (c) 3/32, (d) 4/32, (e) 5/32, (f) 27/32, (g) 28/32, (h) 29/32, (i) 30/32, and (j) 31/32.

observations of similar systems (Smith & Cornell, 1986). However, because the reduced size of the Gly$_2$ carbonyl-carbon chemical shift anisotropy cannot be accurately measured from the simple CPMAS spectrum shown in Figure 8, aspects of gramicidin structure that are reflected in the reduced size of the chemical shift anisotropy cannot be quantified further.

*Mirror-Symmetric 2D REDOR.* Examination of mirror-symmetric, $^{13}$C-observed, $^{15}$N-dephased 2D REDOR spectra of Val$_1$-[1-$^{13}$C]Gly$_2$-[$^{15}$N]Ala$_3$-gramicidin A in a liquid-crystalline, multilamellar DMPC dispersion shows that the only peak that is modulated is the one signifying the presence of Gly$_2$ carbonyl-carbon atoms. Consequently, only the carbonyl-carbon regions of mirror-symmetric 2D REDOR spectra are shown in Figure 9. The acquired $^{13}$C spectra progress from the spectrum displayed in Figure 9a ultimately to the spectrum displayed in Figure 9j as the placement of $^{15}$N $\pi$ pulses is incremented across the rotor cycle.

The carbonyl-carbon magnetization for each $t_1$ point is obtained by integration of the peak centered at 169 ppm and is plotted in Figure 10a as a solid circle. Real Fourier transformation of the $t_1$ time domain in Figure 10a results in the sideband pattern shown in Figure 10b. According to eqs 5 and 6, the modulation of the observed magnetization in Figure 10a and the pattern of sidebands in Figure 10b characterize the magnitude of the effective dipolar coupling constant $|D_e|$ between the Gly$_2$ $^{13}$C-1 carbon and the Ala$_3$ $^{15}$N-amide nitrogen in this multilamellar dispersion. Simulations of the mirror-symmetric data indicate that the magnetization observed as a function of $t_1$ and its Fourier transform are well characterized by a single value of $|D_e|$. These simulations show that the experimental data are best matched to a simulation of observed magnetization (Figure 10a, solid line) and a simulated sideband pattern (Figure 10c) that correspond to an effective dipolar coupling constant of magnitude $|D_e|$ = 260 Hz, with a maximum uncertainty of

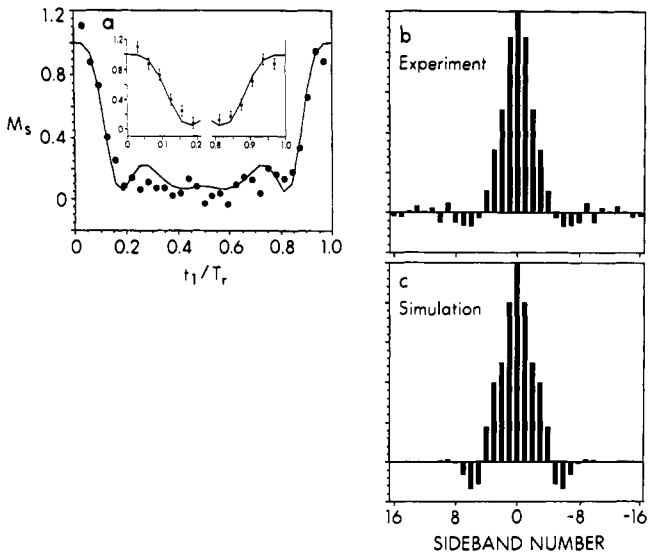


FIGURE 10: Results of the mirror-symmetric experiment performed on $Val_1$-[1-$^{13}$C]$Gly_2$-[$^{15}$N]$Ala_3$-gramicidin A incorporated into a multilamellar DMPC dispersion (Figure 9). Plotted are the experimentally observed magnetization (a, · · ·) and the simulated magnetization (a, —). Fourier transforms of (a, · · ·) and (a, —) are shown in (b) and (c), respectively. The inset in (a) displays an expanded view of the regions corresponding to $t_1/T_r \leq 0.21$ and $t_1/T_r \geq 0.79$. The experimental error bars accompanying each data point plotted in the inset are estimated according to the same procedure used to estimate the error bars of Figure 4a. The simulations assume that $|D_e| = 260$ Hz and that uncoupled $^{13}$C nuclei comprise 9% of the carbons generating signal in the integrated spectral region from 168–170 ppm.

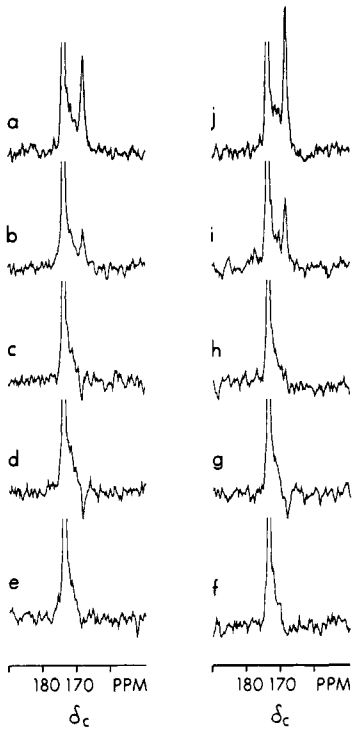


FIGURE 11: Mirror-asymmetric 2D REDOR spectra of a multilamellar DMPC dispersion containing 27 mg of $Val_1$-[1-$^{13}$C]$Gly_2$-[$^{15}$N]-$Ala_3$-gramicidin A at $T = 44$ °C. Mirror-asymmetric spectra were acquired according to the pulse sequence diagrammed in Figure 1d at $1/T_r = 1000$ Hz with $N_c = 16$ and $t_1/T_r$ incremented from 1/32 to 31/32 in steps of 1/32. Spectra from $t_1/T_r = 1/32$ to 10/32 and 22/32 to 31/32 were acquired with 62 464 scans while spectra from $t_1/T_r = 11/32$ to 21/32 were acquired with 8192 scans. Figure 11 displays the spectra corresponding to $t_1/T_r =$ (a) 1/32, (b) 2/32, (c) 3/32, (d) 4/32, (e) 5/32, (f) 27/32, (g) 28/32, (h) 29/32, (i) 30/32, and (j) 31/32.

$\sim\pm$2–3% in the measured value of $|D_e|$ based on the error bars shown in the inset in Figure 10a. Slight deviations of the data from the theoretical simulations may be due to the existence of a very narrow distribution of values centered about the principal $|D_e|$ value or due to the presence of motions other than fast rotation about a given axis.

From the mirror-symmetric determinations of the magnitude of $D_e$ and the magnitude of $D$, values for the angle $\theta$ between the $Gly_2$-$Ala_3$ $^{13}$C–$^{15}$N peptide bond and the motional axis can be calculated from the equation that gives $D_e$ in terms of $D$ and $\theta$, eq 8. However, because only the magnitudes of $D_e$ and $D$ are used in this particular calculation, and because $|D_e|/|D| \leq 1/2$, the equation for $D_e$ yields two pairs of angles as possibilities for $\theta$. Given that $|D_e| = 260$ Hz and $|D| = 1170$ Hz, where $|D|$ is set equal to the average of the mirror-symmetric and mirror-asymmetric results, and the assumption that the only motion present is fast rotation about a given axis, the possible $\theta$ angles are calculated to be two angles and their respective supplements, (46°, 134°) and (64°, 116°). The maximum uncertainty in the calculated values of $\theta$ is $\sim\pm$1° based on the maximum uncertainty of $\sim\pm$2–3% in the measured values of $|D_e|$ and $|D|$. In fact, the calculated $\theta$ angles are not very sensitive to the value of $|D|$ because even if the theoretical value of 1300 Hz is used for the value of $|D|$, the resultant angles are the same to within one degree.

*Mirror-Asymmetric 2D REDOR.* Mirror-asymmetric 2D REDOR spectra of $Val_1$-[1-$^{13}$C]$Gly_2$-[$^{15}$N]$Ala_3$-gramicidin A in a liquid-crystalline, multilamellar DMPC dispersion are shown in Figure 11. As the placement of $^{15}$N $\pi$ pulses is incremented across the rotor cycle, acquired $^{13}$C spectra progress from the spectrum displayed in Figure 11a ultimately to the spectrum displayed in Figure 11j and show how the peak signifying the presence of $Gly_2$ carbonyl-carbon atoms is modulated. Comparison of Figure 11 with Figure 9 shows the difference between the modulation pattern produced by the mirror-asymmetric sequence and the pattern produced by the mirror-symmetric sequence.

The integrated carbonyl-carbon magnetization of the peak centered at 169 ppm is plotted as a function of $t_1$ in Figure 12a as solid circles while the real Fourier transform of these data points is plotted in Figure 12b. According to eqs 5 and 7, the modulation of the observed magnetization in Figure 12a and the pattern of sidebands in Figure 12b characterize the magnitudes and relative sign of the effective dipolar and isotropic indirect spin–spin coupling constants between the $Gly_2$ $^{13}$C-1 carbon and the $Ala_3$ $^{15}$N-amide nitrogen. Since the magnitude of the effective dipolar coupling constant in the multilamellar dispersion is known from the mirror-symmetric experiment to be $|D_e| = 260$ Hz, and since, for reasons stated previously, the magnitude of the isotropic indirect spin–spin coupling constant in the multilamellar dispersion can be assumed to be the same as that in the powder, where $|J| = 14.5$ Hz, the only unknown determinant of the observable magnetization is the relative sign of the effective dipolar and isotropic indirect spin–spin coupling constants. Simulations of the $t_1$ time domain for $D_e$ and $J$ with opposite signs (Figure 12a, solid line) and with identical signs (Figure 12a, dashed line) show that the biggest differences between the opposite-sign and identical-sign simulations occur in the regions where the magnetization is changing most rapidly. Simulations of the Fourier transform of the $t_1$ time domain for $D_e$ and $J$ with opposite signs (Figure 12d) and with identical signs (Figure 12c) therefore show that the biggest differences between the two cases are found in the wings of the Fourier transform. Comparison of these regions of the time-domain and frequency-domain simulations with the corresponding

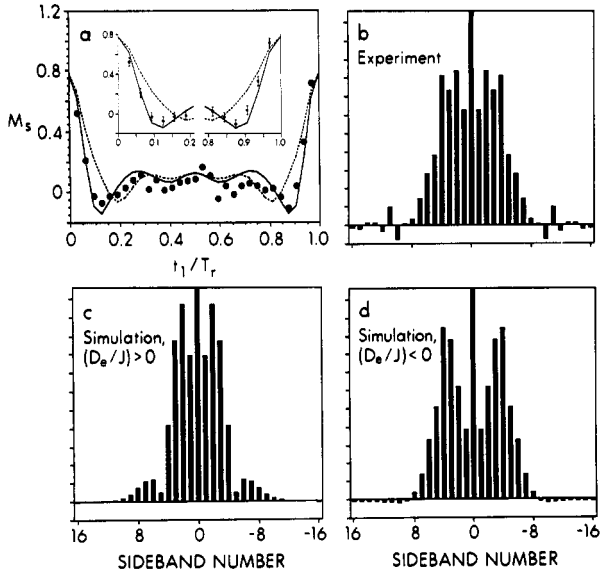


FIGURE 12: Results of the mirror-asymmetric experiment performed on Val$_1$-[1-$^{13}$C]Gly$_2$-[$^{15}$N]Ala$_3$-gramicidin A incorporated into a multilamellar DMPC dispersion (Figure 11). Plotted are the experimentally observed magnetization (a, •••), the simulated magnetization for $D_e$ and J with opposite signs (a, —), and the simulated magnetization for $D_e$ and $J$ with identical signs (a, - - -). Fourier transforms of (a, •••), (a, —), and (a, - - -) are shown in (b), (d), and (c), respectively. The inset in (a) displays an expanded view of the regions corresponding to $t_1/T_r \leq 0.21$ and $t_1/T_r \geq 0.79$. The experimental error bars accompanying each data point plotted in the inset are estimated according to the same procedure used to estimate the error bars of Figure 4a. The simulations assume that $|D_e| = 260$ Hz and $|J| = 14.5$ Hz and that uncoupled $^{13}$C nuclei comprise 13% of the carbons generating signal in the integrated spectral region from 168 to 170 ppm.

regions of the experimental data shows that $D_e$ and $J$ possess opposite signs. Particularly strong support for this conclusion is provided by the inset in Figure 12a, which displays an expanded view of the $t_1$ time domain and plots experimental error bars along with the data points.

The mirror-asymmetric determinations of the relative sign of $D_e$ and $J$ and the relative sign of $D$ and $J$ allow the calculation for the angle $\theta$ between the Gly$_2$-Ala$_3$ $^{13}$C–$^{15}$N peptide bond and the motional axis to be further refined. Specifically, the mirror-asymmetric determination that $D_e$ and $J$ possess opposite signs while $D$ and $J$ possess identical signs indicates that $D_e$ and $D$ possess opposite signs. This conclusion is implicitly based on the fact that $J$ is the value of the isotropic indirect spin–spin coupling constant in a multilamellar dispersion and in a powder sample. Knowledge of the relative sign of $D_e$ and $D$ allows one pair of angles to be eliminated from consideration when $\theta$ is calculated from eq 8. In this case $D_e/D = -(260/1170)$, and so the possible $\theta$ angles are calculated to be a single angle and its supplement (64°, 116°).

## DISCUSSION

*Two-Dimensional REDOR.* The 2D REDOR technique is well suited both experimentally and theoretically to measure the weak $^{13}$C–$^{15}$N dipolar coupling constant $D$ of Val$_1$-[1-$^{13}$C]Gly$_2$-[$^{15}$N]Ala$_3$-gramicidin A in powder samples and the weak effective dipolar coupling constant $D_e$ in multilamellar dispersions. In particular, for multilamellar dispersions possessing an isotropic distribution of motional axis orientations, the theory reduces to a simple form if the rotational rate about the motional axis is much greater than the MAS speed and much greater than the dipolar coupling constant.

Measurement of the magnitudes of the dipolar coupling constants $D$ and $D_e$ is accomplished by straightforward application of the mirror-symmetric 2D REDOR technique. In the final step of the technique, a series of computer simulations is generated for different magnitudes of the dipolar or effective dipolar coupling constant until a best fit to the experimental data is obtained.

Measurement of the signs of the dipolar coupling constants $D$ and $D_e$ relative to the sign of the isotropic indirect spin–spin coupling constant $J$ between Gly$_2$ $^{13}$C-1 and Ala$_3$ $^{15}$N-amide is accomplished by application of the mirror-asymmetric 2D REDOR technique. Analysis of the observable magnetization created by the mirror-asymmetric 2D REDOR sequence is simplified because the magnitudes of the coupling constants are independently determined, and so the only unknown is the sign of the dipolar or effective dipolar coupling constant relative to the sign of the isotropic indirect spin–spin coupling constant. Therefore, only two computer simulations are required to analyze the data: one calculated for coupling constants with opposite signs and one calculated for coupling constants with identical signs. The experimental data must fit either one or the other of these two simulations, and so the only question to be resolved is which simulation fits the experimental data best.

Knowledge of the relative sign of the coupling constants $D$ and $J$ and the relative sign of the coupling constants $D_e$ and $J$ permits the relative sign of $D$ and $D_e$ to be determined since the signs of $D$ and $D_e$ are measured relative to the same quantity, $J$. Although the absolute signs of the coupling constants can be determined ($D$ is negative based on eq 4, therefore $J$ is negative and $D_e$ is positive), only knowledge of their relative signs is required to determine the sign of the order parameter $(3\cos^2\theta - 1)/2$ in eq 8 and calculate the Gly$_2$–Ala$_3$ $^{13}$C–$^{15}$N peptide bond angle $\theta$. Furthermore, the 2D REDOR technique, in contrast to techniques that rely on measuring intensities of MAS sidebands (Kumar et al., 1990), can determine the sign of the order parameter for the case in which the magnitude of $J$ is too small to visibly split MAS sidebands and for the case in which MAS sidebands are not present at all.

*Molecular Conformation.* The 2D REDOR measurements of the effective $^{13}$C–$^{15}$N dipolar coupling constant of Val$_1$-[1-$^{13}$C]Gly$_2$-[$^{15}$N]Ala$_3$-gramicidin A in a liquid-crystalline, multilamellar DMPC dispersion show that a single value of the effective dipolar coupling constant dominates the results. Therefore, only one major conformation of the Gly$_2$–Ala$_3$ $^{13}$C–$^{15}$N peptide bond is present in this system. For this conformation, the experimental results give possible values for the angle $\theta$ between the Gly$_2$–Ala$_3$ $^{13}$C–$^{15}$N peptide bond and the helical axis based on the assumption that fast rotation occurs about the helical axis and is the only motion present. For the lipids surrounding the gramicidin molecules, phosphorus NMR of DMPC head groups verifies formation of a single bilayer phase (Figure 7).

The values experimentally derived in this study for the angle $\theta$ between the Gly$_2$-Ala$_3$ $^{13}$C–$^{15}$N peptide bond and the helical axis allow the various theoretical models proposed for gramicidin structure to be evaluated. Proposed models of double-stranded, helical dimers include the left-handed, antiparallel, $\beta\beta^{5,6}$ helical dimer (species 3); the right-handed, parallel, $\beta\beta^{5,6}$ helical dimer (species 4); the left-handed, parallel, $\beta\beta^{5,6}$ helical dimer that is the mirror image of species 4 (species 1); and the right-handed, antiparallel, $\beta\beta^{7,2}$ helical dimer (Veatch et al., 1974; Prasad & Chandrasekaran, 1977; Colonna-Cesari et al., 1977; Arseniev et al., 1984, 1985a; Bystrov & Arseniev, 1988). Calculation of the angle $\theta$ between the Gly$_2$-Ala$_3$ $^{13}$C–$^{15}$N peptide bond and the helical axis for

each of these models shows that each theoretical $\theta$ value lies within one of two angular ranges, 80–90° or 155–165°. Therefore, these models predict $\theta$ values that are very different from the experimentally derived possibilities for $\theta$, (64°, 116°). Thus, these double-stranded, helical dimer models do not represent the structure of Val$_1$-[1-$^{13}$C]Gly$_2$-[$^{15}$N]Ala$_3$-gramicidin A in a liquid-crystalline, multilamellar DMPC dispersion.

In terms of the single-stranded, $\beta^{6.3}$ helical dimer models (Urry, 1971; Urry et al., 1971; Arseniev et al., 1985b, 1986), calculations show that in the left-handed model, the Gly$_2$-Ala$_3$ $^{13}$C–$^{15}$N peptide bond makes an angle of 139–140° with the helical axis while in the right-handed model, the Gly$_2$-Ala$_3$ $^{13}$C–$^{15}$N peptide bond makes an angle of 61–63° with the helical axis (Venkatachalam & Urry, 1983). Therefore, the experimentally derived possibilities for $\theta$ (64°, 116°) are certainly not consistent with the $\theta$ values predicted by the left-handed, single-stranded, $\beta^{6.3}$ helical dimer model but are consistent with the $\theta$ values predicted by the right-handed, single-stranded, $\beta^{6.3}$ helical dimer model. The certainty with which the left-handed model is eliminated in favor of the right-handed one can be partly attributed to the fact that the angles (46°, 134°) were eliminated from the set of experimentally derived possibilities for $\theta$ by the mirror-asymmetric determinations of the signs of $D$ and $D_e$. Thus, the experimental data argue that the structure of Val$_1$-[1-$^{13}$C]Gly$_2$-[$^{15}$N]Ala$_3$-gramicidin A in a liquid-crystalline, multilamellar DMPC dispersion is that of a right-handed, single-stranded, $\beta^{6.3}$ helical dimer and definitely not that of a left-handed one.

This study's conclusions about overall gramicidin A structure and helical handedness in an unoriented, multilamellar dispersion are in agreement with those of Prosser et al. Although both studies reach the same overall conclusions, they provide complementary information about bond orientations and do so by utilizing different techniques. In this study, 2D REDOR yields information about the $^{13}$C–$^{15}$N peptide bond angle while in the study of Prosser et al., $^2$H NMR yields information about the C$_\alpha$–$^2$H bond angle. Both techniques possess the advantage of being based on an axially symmetric tensor with a known orientation relative to the molecular frame. One further advantage possessed by 2D REDOR is the capability to determine the sign in addition to the magnitude of the observed nuclear spin interaction. Such a capability is important in eliminating possibilities for bond angles and therefore in discriminating between structural models.

The study reported here of Val$_1$-[1-$^{13}$C]Gly$_2$-[$^{15}$N]Ala$_3$-gramicidin A in an unoriented, multilamellar dispersion can also be compared to the work of Cross, whose group has studied the same analog in oriented bilayers (Teng et al., 1991) and whose group has previously documented the helical handedness of gramicidin in oriented bilayers (Nicholson & Cross, 1989). In fact, the 2D REDOR technique of this study and the $^{15}$N NMR method used by Teng et al. yield similar values for the Gly$_2$-Ala$_3$ $^{13}$C-$^{15}$N peptide bond angle relative to the helical axis (64° vs 67°), thereby providing evidence that gramicidin structure in multilamellar dispersions is the same as that in oriented bilayers. However, although both techniques ultimately yield the same information about the Gly$_2$-Ala$_3$ $^{13}$C–$^{15}$N bond angle, their requirements for obtaining this information are different because $^{15}$N NMR spectra of dipolar splittings, unlike 2D REDOR experiments, reveal only the magnitude and not the sign of the interaction. Whereas 2D REDOR examination of only the Gly$_2$-Ala$_3$ $^{13}$C–$^{15}$N dipolar interaction is sufficient to restrict the possibilities for the Gly$_2$-Ala$_3$ $^{13}$C–$^{15}$N bond angle in multilamellar dispersions, $^{15}$N NMR examination of more than just the Gly$_2$-Ala$_3$ $^{15}$N–$^{13}$C dipolar splitting is required to determine the same information in oriented membranes.

## ACKNOWLEDGMENT

Thanks to Dr. Steven P. Adams (formerly of the Monsanto Co., currently at Biogen) for his support and guidance of the gramicidin synthesis performed at the Monsanto Co.

## REFERENCES

Arseniev, A. S., Bystrov, V. F., Ivanov, V. T., & Ovchinnikov, Y. A. (1984) *FEBS Lett. 165*, 51–56.
Arseniev, A. S., Barsukov, I. L., & Bystrov, V. F. (1985a) *FEBS Lett. 180*, 33–39.
Arseniev, A. S., Barsukov, I. L., Bystrov, V. F., Lomize, A. L., & Ovchinnikov, Y. A. (1985b) *FEBS Lett. 186*, 168–174.
Arseniev, A. S., Lomize, A. L., Barsukov, I. L., & Bystrov, V. F. (1986) *Biol. Membr. 3*, 1077–1104.
Bork, V., Gullion, T., Hing, A., & Schaefer, J. (1990) *J. Magn. Reson. 88*, 523–532.
Bystrov, V. F., & Arseniev, A. S. (1988) *Tetrahedron 44*, 925–940.
Chapman, D., Urbina, J., & Keough, K. M. (1974) *J. Biol. Chem. 249*, 2512–2521.
Chapman, D., Cornell, B. A., Eliasz, A. W., & Perry, A. (1977) *J. Mol. Biol. 113*, 517–538.
Colonna-Cesari, F., Premilat, S., Heitz, F., Spach, G., & Lotz, B. (1977) *Macromolecules 10*, 1284–1288.
Cornell, B. A., Separovic, F., Baldassi, A. J., & Smith, R. (1988) *Biophys. J. 53*, 67–76.
Datema, K. P., Pauls, K. P., & Bloom, M. (1986) *Biochemistry 25*, 3796–3803.
Fields, G. B., Fields, C. G., Petefish, J., Van Wart, H. E., & Cross, T. A. (1988) *Proc. Natl. Acad. Sci. U.S.A. 85*, 1384–1388.
Gullion, T., Poliks, M. D., & Schaefer, J. (1988) *J. Magn. Reson. 80*, 553–558.
Gullion, T., & Schaefer, J. (1989) *Adv. Magn. Reson. 13*, 57–83.
Gullion, T., Baker, D. B., & Conradi, M. S. (1990) *J. Magn. Reson. 89*, 479–484.
Hing, A. W., Adams, S. P., Silbert, D. F., & Norberg, R. E. (1990a) *Biochemistry 29*, 4144–4156.
Hing, A. W., Adams, S. P., Silbert, D. F., & Norberg, R. E. (1990b) *Biochemistry 29*, 4156–4166.
Hing, A. W., Vega, S., & Schaefer, J. (1993) *J. Magn. Reson. Ser. A 103*, 151–162.
Hladky, S. B., & Haydon, D. A. (1970) *Nature 225*, 451–453.
Hladky, S. B., & Haydon, D. A. (1972) *Biochim. Biophys. Acta 274*, 294–312.
Irving, C. S., & Lapidot, A. (1976) *J. Chem. Soc., Chem. Commun.* 43–44.
Kainosho, M., Nagao, H., & Tsuji, T. (1987) *Biochemistry 26*, 1068–1075.
Killian, J. A., Nicholson, L. K., & Cross, T. A. (1988) *Biochim. Biophys. Acta 943*, 535–540.
Kricheldorf, H. R. (1980) *Org. Magn. Reson. 14*, 455–461.
Kumar, B. S. A., Ramanathan, K. V., Khetrapal, C. L., Opella, S. J., & Becker, E. D. (1990) *J. Magn. Reson. 86*, 516–525.
LoGrasso, P. V., Nicholson, L. K., & Cross, T. A. (1989) *J. Am. Chem. Soc. 111*, 1910–1912.
Momany, F. A., McGuire, R. F., Burgess, A. W., & Scheraga, H. A. (1975) *J. Phys. Chem. 79*, 2361–2381.
Nicholson, L. K., Moll, F., Mixon, T. E., LoGrasso, P. V., Lay, J. C., & Cross, T. A. (1987) *Biochemistry 26*, 6621–6626.

Nicholson, L. K., & Cross, T. A. (1989) *Biochemistry 28*, 9379–9385.
Nicholson, L. K., Teng, Q., & Cross, T. A. (1991) *J. Mol. Biol. 218*, 621–637.
Power, W. P., & Wasylishen, R. E. (1991) *Annu. Rep. NMR Spectrosc. 23*, 1–84.
Prasad, B. V. V., & Chandrasekaran, R. (1977) *Int. J. Pept. Protein Res. 10*, 129–138.
Prosser, R. S., Davis, J. H., Dahlquist, F. W., & Lindorfer, M. A. (1991) *Biochemistry 30*, 4687–4696.
Rance, M., & Byrd, R. A. (1983) *J. Magn. Reson. 52*, 221–240.
Sarges, R., & Witkop, B. (1965) *J. Am. Chem. Soc. 87*, 2011–2020.
Seelig, J. (1977) *Q. Rev. Biophys. 10*, 353–418.
Seelig, J. (1978) *Biochim. Biophys. Acta 515*, 105–140.
Smith, R., & Cornell, B. A. (1986) *Biophys. J. 49*, 117–118.
Smith, R., Thomas, D. E., Separovic, F., Atkins, A. R., & Cornell, B. A. (1989) *Biophys. J. 56*, 307–314.
Teng, Q., Nicholson, L. K., & Cross, T. A. (1991) *J. Mol. Biol. 218*, 607–619.
Urry, D. W. (1971) *Proc. Natl. Acad. Sci. U.S.A. 68*, 672–676.
Urry, D. W., Goodall, M. C., Glickson, J. D., & Mayers, D. F. (1971) *Proc. Natl. Acad. Sci. U.S.A. 68*, 1907–1911.
Veatch, W. R., Fossel, E. T., & Blout, E. R. (1974) *Biochemistry 13*, 5249–5256.
Venkatachalam, C. M., & Urry, D. W. (1983) *J. Comput. Chem. 4*, 461–469.
Walter, J. A., & Wright, J. L. C. (1979) *Tetrahedron Lett. 41*, 3909–3912.
Witanowski, M., Stefaniak, L., & Webb, G. A. (1986) *Annu. Rep. NMR Spectrosc. 18*, 1–761.